

# In situ visualization of misorientation-dependent hydrogen diffusion at grain boundaries of pure polycrystalline Ni using a hydrogen video imaging system



Hiroshi Kakinuma <sup>a,\*</sup>, Saya Ajito <sup>a</sup>, Tomohiko Hojo <sup>a,b</sup>, Motomichi Koyama <sup>a</sup>, Eiji Akiyama <sup>a</sup>

<sup>a</sup> Institute for Materials Research, Tohoku University, 2-1-1 Katahira, Aoba-ku, Sendai, 980-8577, Japan

<sup>b</sup> Department of Mechanical Engineering and Intelligent Systems, Tohoku Gakuin University, 3-1 Shimizukoji, Wakabayashi-ku, Sendai, 984-8588, Japan

---

## ARTICLE INFO

### Keywords:

Hydrogen video imaging  
 Hydrogen-material interactions  
 Hydrogen diffusion  
 Polycrystalline metals

---

## ABSTRACT

Hydrogen, the key element for solving the major environmental issues, exhibits rapid diffusion and localization in lattice defects of metals, which leads to embrittlement. However, the microstructure-hydrogen interactions in metallic materials are poorly understood. Therefore, a technique for capturing the microstructure-dependent hydrogen diffusion in real-time has long been targeted by researchers. Here, we successfully visualized the preferential hydrogen diffusion at grain boundaries (GBs) of pure Ni using a hydrogen video imaging system. A thin polyaniline layer was utilized as a hydrogenochromic sensor, and the hydrogen distribution was analyzed based on the color distribution of polyaniline. The system revealed the misorientation-dependent hydrogen flux at GBs of pure polycrystalline Ni with a micrometer-scale spatial resolution. It suggests that the geometrical structure of the GBs is a critical factor for preferential hydrogen diffusion. The use of the hydrogen video imaging system further advances the mechanistic understanding of hydrogen-material atomic interactions in polycrystalline metals and critically facilitates the development of hydrogen-related materials.

## 1. Introduction

Infrastructural materials for the hydrogen energy society include hydrogen-permeable membranes [1,2], hydrogen storage materials [3, 4], and hydrogen-resistant alloys [5,6]. The hydrogen-material interactions have been extensively studied: hydrogen entry into materials [7], diffusion and localization of hydrogen in materials [8,9], hydrogen-altered lattice defect motion/evolution [10,11], etc., which are dependent on the microstructure of the materials. However, the microstructure-hydrogen interactions are not clearly understood; for example, it is still discussed whether the grain boundaries (GBs) of metals could be barriers to hydrogen diffusion or preferential hydrogen diffusion paths [12–18]. A main obstacle to understanding the microstructure-hydrogen interaction is the difficulty of detecting the atomic state hydrogen in metals. In addition, there are microstructural inhomogeneities, such as grain boundaries, crystal orientations, inclusions, and elemental segregations, in practical materials. Thus, it is required to observe the hydrogen distribution of the sub-millimeter-scale observation area, which contains a lot of grains, with high spatial and temporal resolutions to determine the

microstructure-hydrogen interactions.

Scanning Kelvin probe force microscopy (SKPFM) [19], scanning Kelvin probe (SKP) [20,21], hydrogen microprint (HMT) [22], secondary ion mass spectrometry (SIMS) [23], and silver decoration methods (Ag) [24] are typical approaches that can analyze the hydrogen distribution of sub-millimeter-scale observation area. These visualization techniques exhibit a high spatial resolution. However, it is still challenging to analyze a sub-millimeter-scale observation area with high spatial and temporal resolutions. Both the micrometer-scale spatial and sub-second-scale (video-rate) temporal resolutions are required to elucidate the microstructure-hydrogen interactions. In this study, we developed a hydrogen video imaging system (HVIS) to break the technical limitations. Fig. 1a shows the mechanism of the hydrogen visualization. Hydrogen is electrochemically introduced into the specimen (Ni film in this study), and the atomic state hydrogen diffuses in the Ni film, reaching the other side. On the other side, a thin polyaniline layer (PANI) is polymerized as a hydrogenochromic sensor. Since the color of PANI changes from purple and dark blue to yellow and white due to the reaction with the atomic state hydrogen [25], the hydrogen diffusion behavior in the Ni film can be analyzed based on the color change of

\* Correspondence author.

E-mail address: [hiroshi.kakinuma.a1@tohoku.ac.jp](mailto:hiroshi.kakinuma.a1@tohoku.ac.jp) (H. Kakinuma).

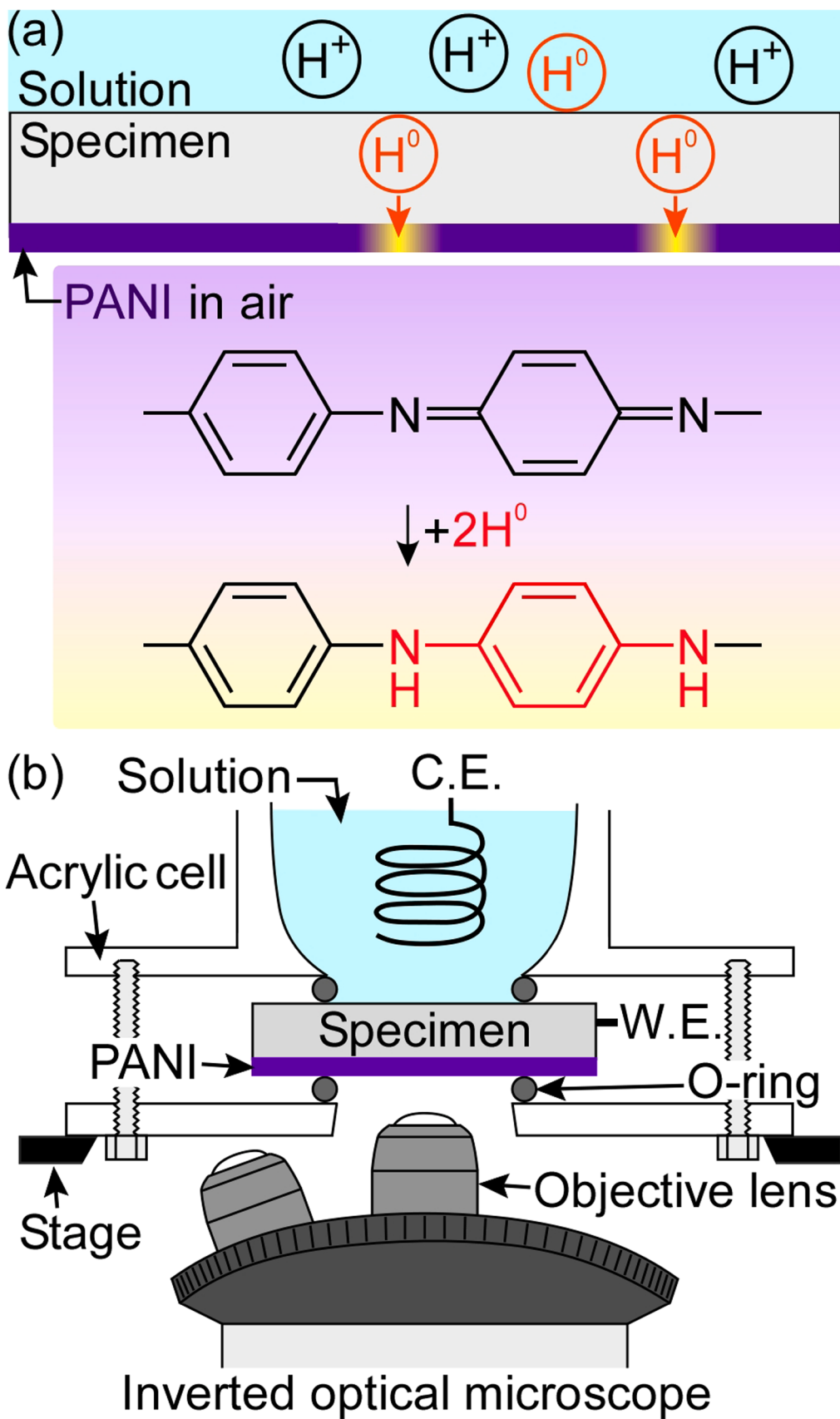


Fig. 1. Schematics of (a) the principle and (b) the experimental setup of HVIS.

PANI.

In this study, the HVIS successfully visualized the microstructure-dependent hydrogen distribution in pure polycrystalline Ni with a micrometer-scale spatial resolution. The hydrogen diffusion behavior in pure polycrystalline Ni, which has been long discussed, was experimentally determined: the random GBs of pure polycrystalline Ni are the preferential hydrogen diffusion paths. Furthermore, the hydrogen flux at the GBs was found to depend on the misorientation angle, indicating that the geometrical structure of the GBs is a critical factor for the hydrogen flux. The HVIS paves the way for elucidating the hydrogen diffusion behavior in polycrystalline metals in correlation with their microstructure.

## 2. Experimental

### 2.1. Specimens and characterization

Pure polycrystalline Ni (99.9 %) with a thickness of 125  $\mu\text{m}$  was annealed under vacuum at 1273 K for 1 h and cooled to 873 K. Subsequently, the specimen was kept at 873 K for 24 h. The pure Ni specimen was electrically polished at 50 V in a mixed solution of acetic acid (60 mass%, 210 mL) and perchloric acid (99.7 mass%, 790 mL). The final film thickness was approximately 110  $\mu\text{m}$ . PANI was electrically polymerized on one side of the pure Ni at a constant voltage of 1 V for 150 s in 0.5 M  $\text{H}_2\text{SO}_4$ -0.5 M aniline aqueous solution (150 mL). After polymerization, the specimen was rinsed with distilled water and dried with  $\text{N}_2$  gas.

PANI on the pure Ni specimen was cut using a focused ion beam (FIB) to observe the cross-section of the specimen. The morphology of the cross-section of the specimen was analyzed using transmission electron microscopy (TEM). After hydrogen visualization, PANI was removed by immersing the specimens in a 1 M NaOH solution. The microstructure of the specimen was analyzed using the electron back-scatter diffraction (EBSD) method at an accelerating voltage of 20 kV. Because the EBSD image was taken at a tilted angle of 70°, the size and aspect ratio can be slightly different between the EBSD images and optical micrographs. Thus, the size and aspect ratio of the EBSD image were adjusted according to the optical images.

The absorption spectrum of PANI on pure Ni was measured using a UV-visible spectrometer. For the first 24 h, the spectrum of PANI was measured in the air without hydrogen charging. Subsequently, hydrogen charging was conducted from the other side of the specimen at a constant current density of  $-10 \text{ A m}^{-2}$  in 0.1 M NaOH for 120 h. The electrode area was approximately 0.5  $\text{cm}^2$ , and a Pt wire was used as a counter electrode.

### 2.2. Hydrogen video imaging system

**Fig. 1b** shows the experimental setup of the HVIS. The upper side of the specimen was exposed to a 0.1 M NaOH solution to introduce hydrogen by galvanostatic polarization. As a hydrogenochromic sensor [25], PANI was polymerized on the other side. The color change of PANI was monitored using an inverted optical microscope. An objective lens with a magnification of  $\times 20$  was used. The numerical aperture of the objective lens was 0.45, so the theoretical resolution of the images can be calculated as 0.75  $\mu\text{m}$ . The optical micrographs of PANI were captured every 0.5 h during hydrogen charging for 120 h. Prior to hydrogen charging, optical micrographs were taken for 20 h to confirm the stability of the color of PANI under the observation condition. Hydrogen charging was conducted at a constant current density of  $-10 \text{ A m}^{-2}$  in a 0.1 M NaOH aqueous solution. The electrode area of the working electrode (W.E.) was approximately 0.5  $\text{cm}^2$ , and a Pt wire was used as the counter electrode (C.E.).

## 3. Results and discussion

### 3.1. Morphology of PANI polymerized on a pure polycrystalline Ni film

In this study, a pure polycrystalline Ni film was used as a specimen to verify whether the GBs of pure Ni act as preferential hydrogen diffusion paths. The microstructure of the Ni was obtained by EBSD. The average grain size was approximately 20  $\mu\text{m}$  (see Supplemental Figure 1 for more information on the number fraction of grain size and misorientation angle). To analyze the microstructure-dependent hydrogen diffusion, it is necessary to confirm that the morphology of PANI does not depend on the microstructure of polycrystalline Ni. **Fig. 2a** and b are TEM and high-resolution TEM images of the cross-section around the Ni-PANI interface. As shown in **Fig. 2a**, PANI was uniformly formed on both GB and grain interiors. Furthermore, the structure of PANI was independent of the microstructure of polycrystalline Ni (**Fig. 2b**). **Fig. 2c** shows the absorption spectra of PANI. The blue and green curves indicate the absorption spectrum before and after the storage in ambient air for 24 h, respectively. The color of PANI was confirmed to be stable under the present observation conditions when hydrogen was not introduced. After the storage in ambient air, hydrogen charging was conducted. The red curve in **Fig. 2c** shows the absorption spectrum of PANI after hydrogen charging. The absorption spectrum was significantly changed after hydrogen charging, indicating that the PANI layer fabricated on the Ni visualizes the hydrogen permeated through the Ni film.

### 3.2. Visualizing the microstructure-dependent hydrogen diffusion behavior in polycrystalline Ni

Visualization of the microscopic hydrogen diffusion behavior in the pure polycrystalline Ni was attempted using the HVIS. The color of PANI under the experimental condition was confirmed to be stable before hydrogen charging even on the microscopic scale (see Supplemental Figure 2). **Fig. 3a** shows the optical micrographs of PANI before and during hydrogen charging. A scratch, indicated by the yellow arrow, was made to synchronize the position in multiple optical micrographs. Before hydrogen charging, the color of PANI was purple. After 20 h of

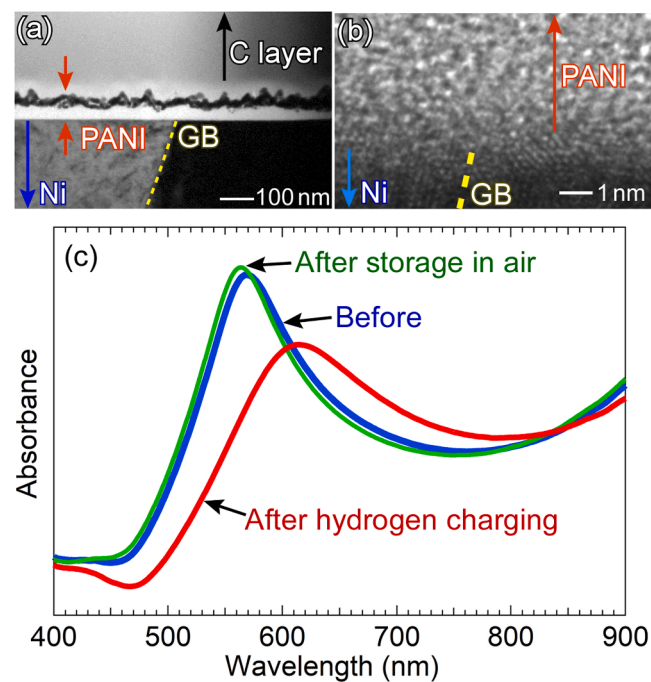


**Fig. 2.** (a) TEM image and (b) high-resolution TEM image of the cross-section of the Ni-PANI interface. (c) Absorption spectra of PANI on pure Ni before and after storage in ambient air for 24 h and after hydrogen charging for 120 h.

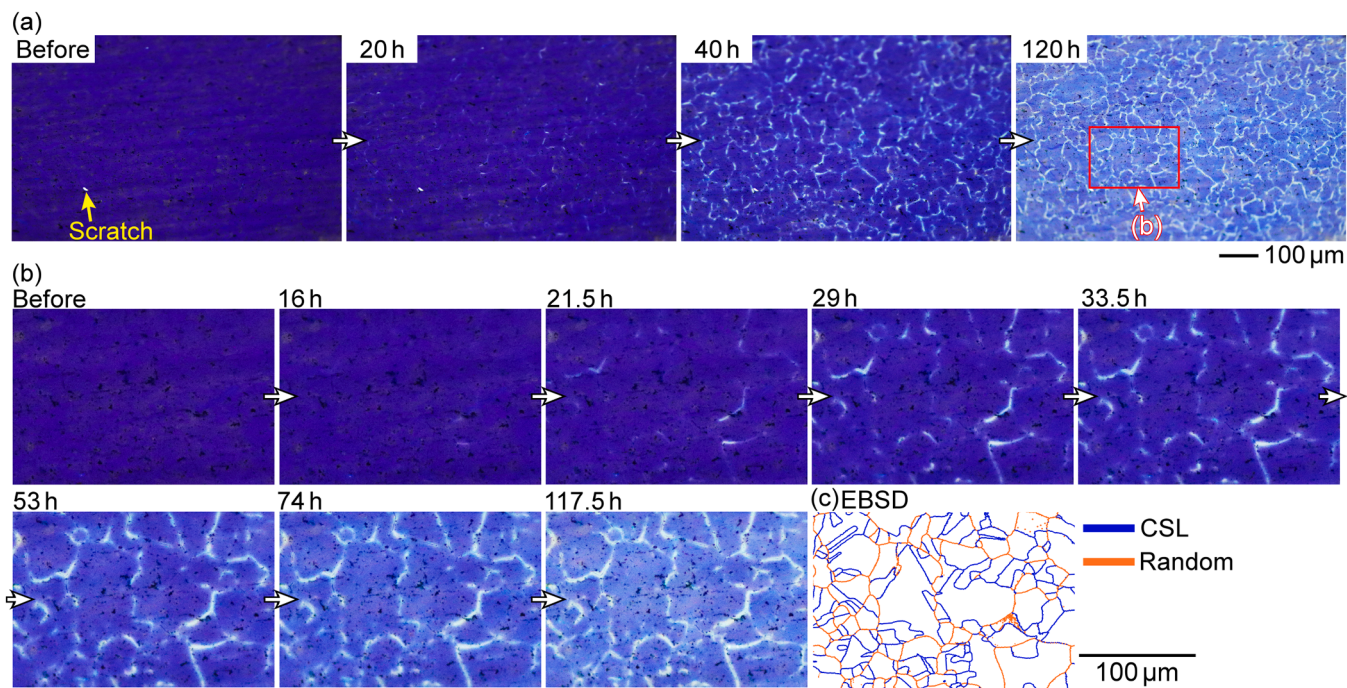


**Fig. 3.** (a) Optical micrographs of PANI before and during hydrogen charging. A scratch, indicated by the yellow arrow, was made to synchronize the positions in multiple optical micrographs. (b) Enlarged views and (c) GBs of the pure Ni of the area indicated by the red rectangle in (a).

hydrogen charging, the color of PANI turned white locally, indicating the detection of hydrogen. Because the color change of PANI corresponds to the integrated value of the hydrogen flux (see Supplemental Figure 3), the whitening (the degree of the color change from purple to white) indicates a large hydrogen flux in that area. The number of white areas increased over time.

Fig. 3b shows the local color change of PANI during hydrogen charging in the area indicated by the red rectangle in Fig. 3a. The color of PANI started to turn white locally in 16 h. The white areas became brighter and the number of white areas increased with time. Notably, the shape of the white areas was short line segments. After 53 h, the increase in the number of white areas became moderate, and the color of the entire observation area gradually brightened. Fig. 3c shows the GBs of the Ni in the same observation area of Fig. 3b. By comparing Fig. 3b and c, the whitening was found to occur at the GBs, indicating that the hydrogen flux at the GBs is larger than that inside the grains. Hereafter, the brighter area is called the higher hydrogen flux area. The optical micrographs in Fig. 3a and b were converted into video information (see Supplemental Video 1 and Video 2). In Fig. 3c, the blue and orange curves indicate the coincidence site lattice grain boundaries (CSLs: Σ3–Σ19) and random GBs, respectively. The hydrogen flux at the random GBs seemed to be larger than that at the CSLs, suggesting that the hydrogen flux depends on the character of the GBs.

Fig. 4a shows an optical micrograph of the area shown in Fig. 3b after 120 h of hydrogen charging. The red portions shown in Fig. 4b highlight the higher hydrogen flux areas in the binarized image. Fig. 4c and e show the CSLs and random GBs of the Ni from the same area shown in Fig. 4a. To analyze the positional relationship between the GBs and higher hydrogen flux areas, Fig. 4c and e were superimposed on Fig. 4b, and the superimposed images are shown in Fig. 4d and f, respectively. The CSLs (blue curves) and the higher hydrogen flux areas (red areas) did not overlap each other in Fig. 4d, while most of the higher hydrogen flux areas overlapped with the random GBs (Fig. 4f).

From the results above, it was found that the hydrogen flux in the polycrystalline Ni depends on the microstructure and that hydrogen tends to diffuse through the GBs preferentially. Furthermore, the hydrogen flux at the random GBs was larger than that at the CSLs. As

shown in Fig. 4f, not all random GBs overlapped with the red areas (higher hydrogen flux areas), suggesting that there is a difference in hydrogen flux among the random GBs.

### 3.3. Quantitative analyses of the hydrogen flux at each GB

Fig. 5a and b show the optical micrographs of PANI and the EBSD images of the polycrystalline Ni shown in Figs. 4a and 3c, respectively. Areas 1–4 (red and black rectangles in Fig. 5a and b) contain the CSL ( $\Sigma 3$  GB), the inside of the grain, the random GB, and the whole observation area, respectively. To quantitatively analyze the temporal variations of the color change in Areas 1–4, the values of  $R$  (red),  $G$  (green), and  $B$  (blue) of each pixel inside the areas were extracted (the number of pixels in Areas 1–4 was 196, 576, 169, and 422,940 respectively), and the brightness  $Y$  was calculated using the following equation.

$$Y = 0.229R + 0.587G + 0.114B \quad (1)$$

$Y$  is widely used to quantify the brightness of objects [26]. Fig. 5c shows the temporal variation of the average change in brightness ( $\Delta Y$ ) value in Areas 1–4.  $\Delta Y$  was calculated using the following equation:

$$\Delta Y = Y_t - Y_0 \quad (2)$$

$\Delta Y$  refers to the difference between the value at time  $t$  ( $Y_t$ ) and the value before hydrogen charging ( $Y_0$ ). The  $\Delta Y$  value was confirmed to correspond to the integrated value of hydrogen flux (see Supplemental Figure 3). At the random GB (Area 3),  $\Delta Y$  began to increase sharply after 16 h, and the increase in  $\Delta Y$  became moderate after 30 h. Because the  $\Delta Y$  value barely increased after 100 h, it seemed that the upper limit of the  $\Delta Y$  value of the PANI layer was approximately 160 to 170. The little increase in  $\Delta Y$  may be due to the fact that polyaniline has been hydrogenated and the yield of further hydrogenation has decreased. The temporal variations of  $\Delta Y$  inside the grain (Area 2) or at the  $\Sigma 3$  GB (Area 1) were almost the same. After 18 h,  $\Delta Y$  in Areas 1 and 2 increased gradually and continuously. These results show that the hydrogen flux at the random GB is larger than at the  $\Sigma 3$  GB and that the hydrogen flux inside the grain is almost the same as that of the  $\Sigma 3$  GB. Moreover,  $\Delta Y$  in Area 4 (the whole observation area) was almost the same as in Areas 1

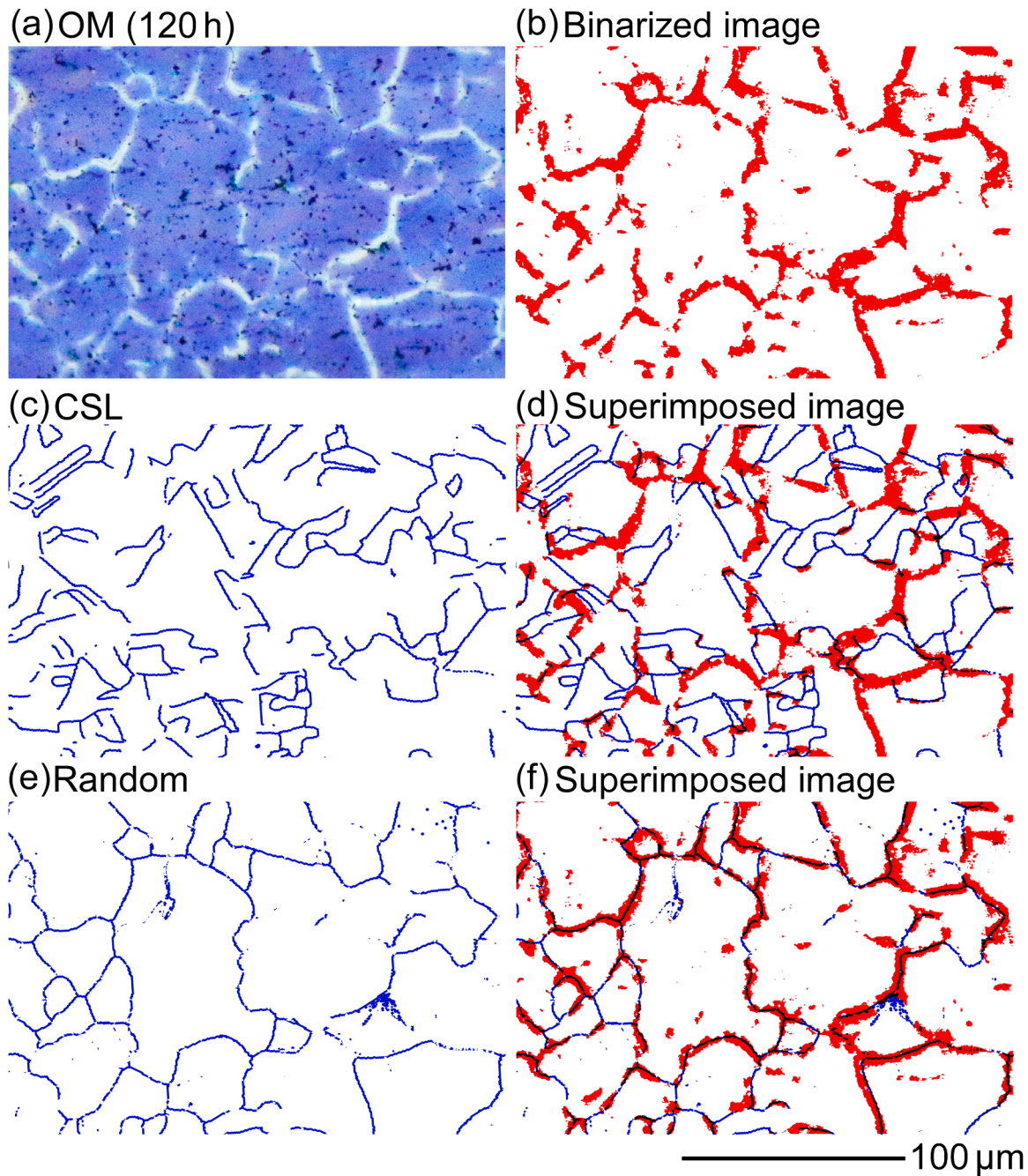


**Fig. 4.** (a) Optical micrograph (OM) of PANI after hydrogen charging for 120 h. (b) Binarized image of (a). (c) CSLs and (e) random GBs of the area shown in (a). (d) Superimposed image of the images shown in (b) and (c). (f) Superimposed image of the images shown in (b) and (e).

and 2, implying that the average value of the hydrogen flux hardly reflects the high hydrogen flux around the random GBs. To determine the microstructure-dependent hydrogen flux in metals, it is important to analyze the local hydrogen diffusion behavior with a two-dimensional spatial resolution.

In addition to GBs, metals have various inhomogeneities, such as dislocation distribution, localized strain, and elemental segregation. Therefore, to determine the role of GBs in hydrogen flux, it is necessary to confirm the reproducibility of the results. Each pixel of the optical micrographs shown in Fig. 3b was extracted and  $\Delta Y$  was calculated by the same procedure, as shown in Fig. 5. Fig. 6a shows the contour maps of  $\Delta Y$ . The GBs of polycrystalline Ni obtained by EBSD are also shown as a reference (EBSD data in Fig. 6a). The color of the GBs indicates the misorientation angle,  $\theta$ . In this study, the misorientation angle was

defined as the difference in the Euler angle between the two grains. As shown in the contour maps, hydrogen was detected at some of the GBs after 20 h of hydrogen charging. The  $\Delta Y$  value was approximately 60–80. After 60 h, the increase in  $\Delta Y$  was detected even inside the grains, followed by the continuous increase in  $\Delta Y$  over time.

Since the  $\Delta Y$  value, which increased monotonically during hydrogen charging (Fig. 5c), corresponds to the integrated value of hydrogen flux, the hydrogen flux at each GB can be analyzed by comparing the increasing rate of  $\Delta Y$ . Then, the time when the  $\Delta Y$  value reached 60 ( $t_{\Delta Y 60}$ ) was calculated at each GB. Fig. 6b shows  $t_{\Delta Y 60}$  of the GBs with a length of more than 10  $\mu\text{m}$  inside the observation area shown in Fig. 6a. The smallest value of  $t_{\Delta Y 60}$  was confirmed at the GBs with a misorientation of  $30^\circ \leq \theta < 40^\circ$ , meaning that the hydrogen flux at the GBs was the largest. Furthermore, the hydrogen flux at the GBs with a

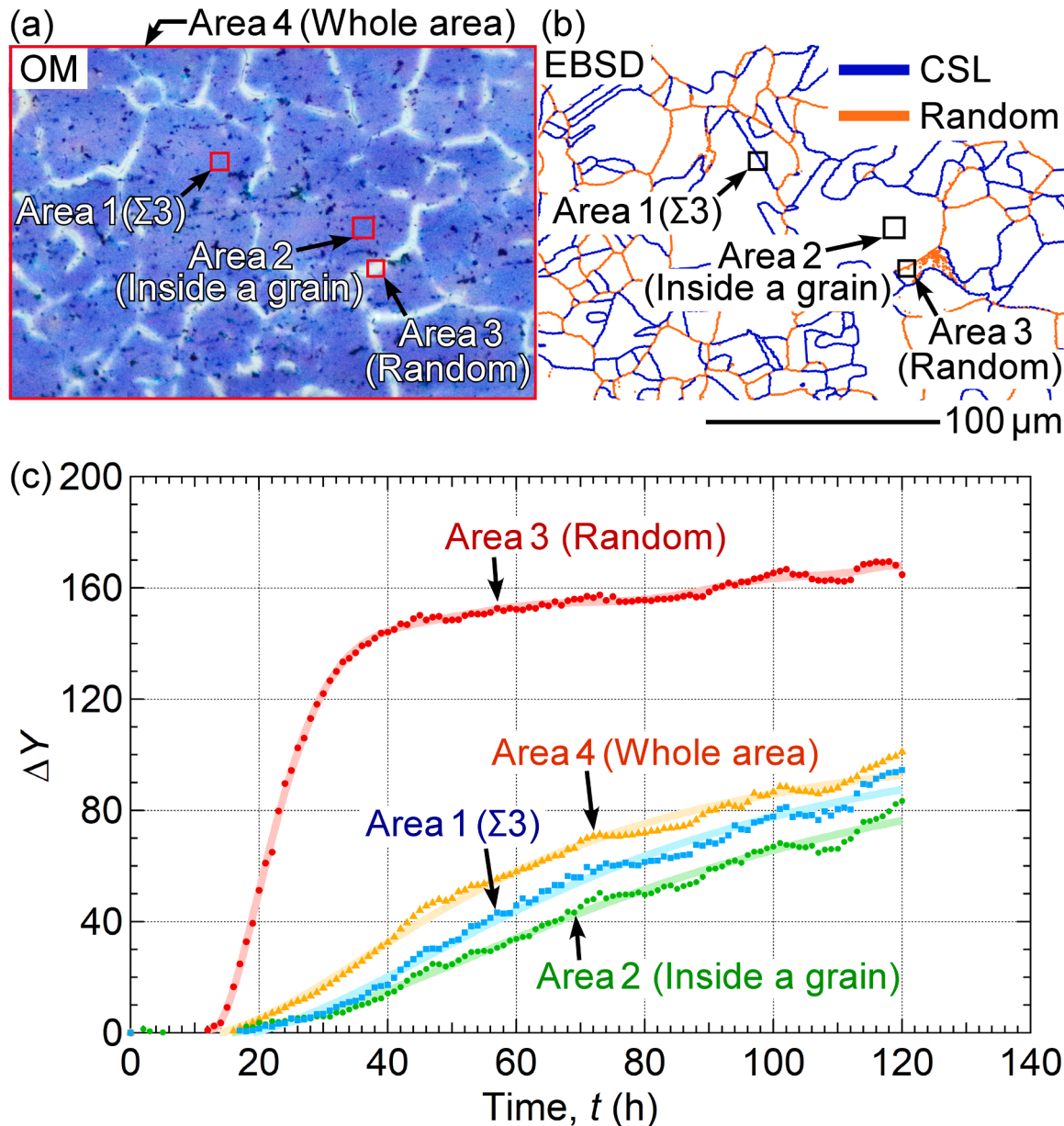


**Fig. 5.** (a) Optical micrograph of PANI shown in Fig. 4a and (b) CSLs and random GBs of the corresponding area obtained by EBSD. (c) Temporal variations of the average  $\Delta Y$  in Areas 1–4 indicated by the red rectangles in (a).

misorientation of  $40^\circ \leq \theta < 50^\circ$  was higher than those with misorientations of  $15^\circ \leq \theta < 30^\circ$  and  $50^\circ \leq \theta \leq 58^\circ$ . Since  $t_{\Delta Y 60}$  inside the grains was approximately 90 h, it was found that the hydrogen flux in the low angle GBs ( $10^\circ \leq \theta < 15^\circ$ ) is higher than that inside the grains. There were also  $\Sigma 9$  GBs in the range of  $30^\circ \leq \theta < 50^\circ$ , and  $t_{\Delta Y 60}$  at the  $\Sigma 9$  GBs was relatively longer than the other random GBs with a misorientation of  $30^\circ \leq \theta < 50^\circ$ . However, there were only three  $\Sigma 9$  GBs in the observation area, implying that further statistical analysis is required to determine the difference in the hydrogen flux between the random and  $\Sigma 9$  GBs. In addition, the low-angle GBs ( $10^\circ \leq \theta < 15^\circ$ ) had the smallest hydrogen flux among the random GBs, but it was higher than that of  $\Sigma 3$  GB, clarifying that the hydrogen flux at the random GBs is higher than  $\Sigma 3$  GBs. The number of coincidence sites in a particular CSL (value of  $\Sigma$ ) and misorientation,  $\theta$ , are confirmed to be important factors governing the hydrogen flux at the GBs. First-principle calculations and kinetic Monte Carlo simulations performed by Zhou et al. [27] estimated that the GBs of Ni are the preferential diffusion path for hydrogen atoms. They calculated the hydrogen diffusivity of the GBs based on the

Frank-Bilby model and suggested that the hydrogen diffusivity depends on  $\theta$ . According to the Frank-Bilby model [28,29], the intrinsic net defect density of a GB monotonically increases with the increase in  $\theta$  in the range of  $\theta < 36.87^\circ$  and monotonically decreases in the range of  $36.87^\circ < \theta < 90^\circ$ . This tendency is in good agreement with the misorientation-dependence of hydrogen flux that becomes maximum in the range of  $30^\circ \leq \theta < 40^\circ$ . Thus, it is suggested that the hydrogen flux at the GBs in Ni changes depending on the geometrical structure of the GBs.

Fig. 6c and d show the contour map of  $\Delta Y$  of PANI and the GB map of polycrystalline Ni in the area indicated by the white rectangle in Fig. 6a. The color of the GBs indicates the misorientation angle, as shown in EBSD data in Fig. 6a. When comparing Fig. 6c and d, it is clear that the increase in  $\Delta Y$  occurred mainly around random GBs. Fig. 6e and f show the line profiles of  $\Delta Y$  on Lines 1 and 2 indicated in Fig. 6c and d. After 20 h of hydrogen charging,  $\Delta Y$  began to increase around the GB ( $\theta = 34^\circ$ ) and continued to increase over time. After 30 h,  $\Delta Y$  inside the grains gradually increased. Furthermore, the half-width of the peak of

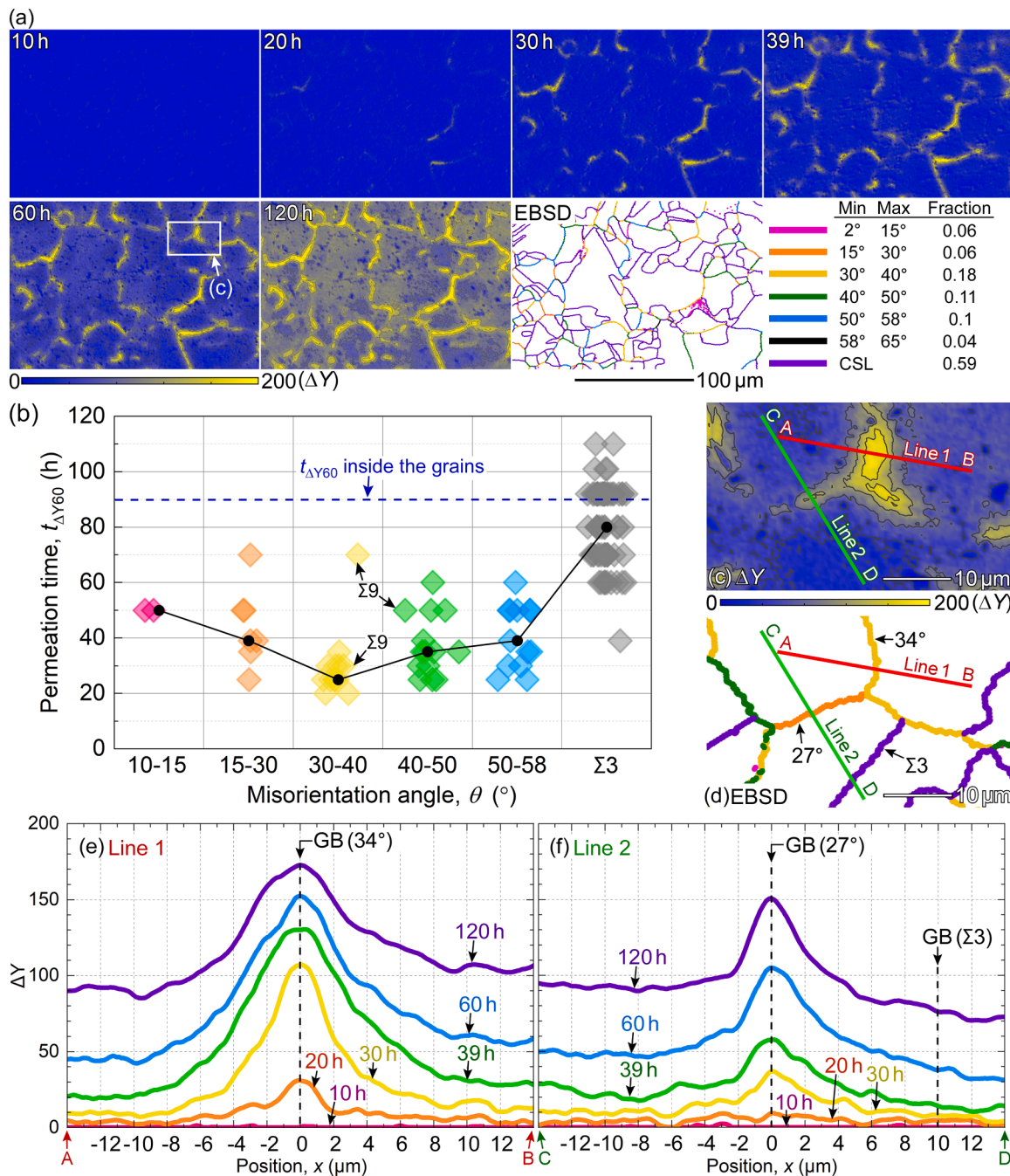


**Fig. 6.** (a) Contour maps of the  $\Delta Y$  value obtained from the optical micrographs shown in Fig. 3b and the GBs of the corresponding area of the pure Ni. (b) Permeation time ( $t_{\Delta Y60}$ ) of each GB with a length of more than 10  $\mu\text{m}$  in the area shown in (a). (c) Enlarged contour map of the  $\Delta Y$  value and (d) GBs of the pure Ni in the area indicated by the white rectangle in (a). Temporal variations of the line profile of the  $\Delta Y$  value at the positions indicated by (e) the red (Line 1) and (f) green (Line 2) lines in (c) and (d).

$\Delta Y$  at the random GB increased with time, indicating that hydrogen in the random GB diffused to the inside of the grains. As shown in Fig. 6f, a similar tendency was confirmed even at the GB ( $\theta = 27^\circ$ ). However, no peak of the  $\Delta Y$  value was confirmed at the  $\Sigma 3$  GB, implying that the hydrogen flux at the  $\Sigma 3$  GBs was almost the same as that inside the grains.

In this study, we developed the HVIS to visualize the hydrogen distribution of the sub-millimeter-scale observation area with a micrometer spatial resolution. The HVIS successfully visualized the misorientation-dependent hydrogen diffusion at GBs of pure Ni. These findings seem to be related to practical problems such as blister formation at GBs that also show a similar misorientation dependence [30], but further

investigation is required to clarify the role of the hydrogen flux in the blistering. Since the color of the hydrogenochromic sensor is observed using visible light, the temporal resolution of HVIS depends on neither the observation area nor spatial resolution. Therefore, HVIS can be applied to an even wider field of view observation with a video-rate temporal resolution. As shown in Fig. 7, the temporal and spatial resolutions of HVIS are higher than the conventional hydrogen visualization techniques for the sub-millimeter-scale observation area. It is thought that HVIS can reveal the microstructure-dependent hydrogen diffusion behavior in a metal, which has a large hydrogen diffusion coefficient.

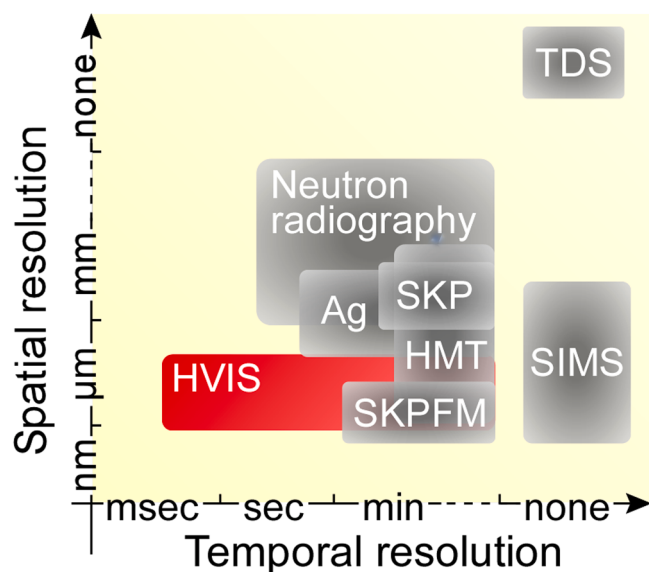


**Fig. 7.** Spatial and temporal resolutions of the HVIS and the other hydrogen analysis techniques for more than sub-millimeter-scale observation area.

#### 4. Conclusions

In this study, the microstructure-dependent hydrogen diffusion behavior in polycrystalline Ni was visualized *in situ* using a hydrogen video imaging system (HVIS). HVIS revealed that the hydrogen flux at the grain boundaries (GBs) depends on GB character (the values of  $\Sigma$  and misorientation angle,  $\theta$ ), indicating that the geometrical structure of GBs is a critical factor for the hydrogen flux. Hence, the HVIS provides a pathway to gain new insight into the microstructural hydrogen kinetics in solids, which opens a new venue for GB character-based design of hydrogen-related structural and functional materials.

1. The structure of PANI was independent of the microstructure of polycrystalline Ni.
2. The color of PANI was confirmed to be stable under the irradiation of UV-visible light in ambient air, while the absorption spectrum PANI was significantly changed after hydrogen charging, indicating that the PANI layer fabricated on pure polycrystalline Ni visualizes the hydrogen permeated through the Ni film.
3. The hydrogen flux in the polycrystalline Ni depended on the microstructure. Atomic state hydrogen in the polycrystalline Ni diffused through the GBs preferentially, and the hydrogen flux at the random GBs was larger than that at the  $\Sigma 3$  GBs.
4. The hydrogen flux inside the grains was almost the same as that of the  $\Sigma 3$  GBs.
5. The largest hydrogen flux was confirmed at the GBs with a misorientation of  $30^\circ \leq \theta < 40^\circ$ . Furthermore, the hydrogen flux at the GBs with a misorientation of  $40^\circ \leq \theta < 50^\circ$  was higher than those with misorientations of  $15^\circ \leq \theta < 30^\circ$  and  $50^\circ \leq \theta \leq 58^\circ$ . The low-angle GBs ( $10^\circ \leq \theta < 15^\circ$ ) had the smallest hydrogen flux among the random GBs, but it was higher than that of  $\Sigma 3$  GB, clarifying that the values of  $\Sigma$  and  $\theta$  are confirmed to be important factors governing the hydrogen flux at the GBs.

#### Declaration of Competing Interest

The authors declare that they have no known competing financial interests or personal relationships that could have appeared to influence the work reported in this paper.

#### Acknowledgements

We thank K. Kobayashi for his assistance in performing SEM-FIB and TEM experiments. This work was supported by a cooperative program of Collaborative Research and Development Center for Advanced Materials at Institute for Materials Research, Tohoku University (No. 202112-CRKKE-0410) and JSPS KAKENHI Grants-in-Aid for Scientific Research on Innovative Areas “Hydrogenomics”, JP18H05514.

#### Supplementary materials

Supplementary material associated with this article can be found, in the online version, at doi:10.1016/j.actamat.2023.119536.

#### References

- [1] N.W. Ockwig, T.M. Nenoff, Membranes for hydrogen separation, Chem. Rev. 107 (2007) 4078–4110, <https://doi.org/10.1021/cr050179z>.
- [2] S.K. Gade, S.J. Chmelka, S. Parks, J.D. Way, C.A. Wolden, Dense carbide/metal composite membranes for hydrogen separations without platinum group metals, Adv. Mater. 23 (2011) 3585–3589, <https://doi.org/10.1002/adma.201100931>.
- [3] G. Xia, Y. Tan, X. Chen, F. Fang, D. Sun, X. Li, Z. Guo, X. Yu, Oxygen-free layer-by-layer assembly of lithiated composites on graphene for advanced hydrogen storage, Adv. Sci. 4 (2017), 1600257, <https://doi.org/10.1002/advs.201600257>.
- [4] Q. Sun, N. Wang, Q. Xu, J. Yu, Nanopore-supported metal nanocatalysts for efficient hydrogen generation from liquid-phase chemical hydrogen storage materials, Adv. Mater. 32 (2020), 2001818, <https://doi.org/10.1002/adma.202001818>.
- [5] B. Sun, W. Lu, B. Gault, R. Ding, S.K. Makineni, D. Wan, C.-H. Wu, H. Chen, D. Ponge, D. Raabe, Chemical heterogeneity enhances hydrogen resistance in high-strength steels, Nat. Mater. 20 (2021) 1629–1634, <https://doi.org/10.1038/s41563-021-01050-y>.
- [6] H. Luo, S.S. Sohn, W. Lu, L. Li, X. Li, C.K. Soundararajan, W. Krieger, Z. Li, D. Raabe, A strong and ductile medium-entropy alloy resists hydrogen embrittlement and corrosion, Nat. Commun. 11 (2020) 3081, <https://doi.org/10.1038/s41467-020-16791-8>.
- [7] E. Akiyama, K. Matsukado, M. Wang, K. Tsuzaki, Evaluation of hydrogen entry into high strength steel under atmospheric corrosion, Corros. Sci. 52 (2000) 2758–2765, <https://doi.org/10.1016/j.corsci.2009.11.046>.
- [8] M. Dadfarnia, P. Novak, D.C. Ahn, J.B. Liu, P. Sofronis, D.D. Johnson, I. M. Robertson, Recent advances in the study of structural materials compatibility with hydrogen, Adv. Mater. 22 (2010) 1128–1135, <https://doi.org/10.1002/adma.200904354>.
- [9] C.R. O’Connor, M.A. Spronken, T. Egle, F. Xu, H.R. Kersell, J. Oliver-Meseguer, M. Karatok, M. Salmon, R.J. Madix, C.M. Friend, Hydrogen migration at restructuring palladium–silver oxide boundaries dramatically enhances reduction rate of silver oxide, Nat. Commun. 11 (2020) 1844, <https://doi.org/10.1038/s41467-020-15536-x>.
- [10] I.M. Robertson, P. Sofronis, A. Nagao, M.L. Martin, S. Wang, D.W. Gross, K. E. Nygren, Hydrogen embrittlement understood, Metall. Mater. Trans. A 46 (2015) 2323–2341, <https://doi.org/10.1007/s11661-015-2836-1>.
- [11] M. Nagumo, K. Takai, The predominant role of strain-induced vacancies in hydrogen embrittlement of steels: overview, Acta Mater. 165 (2019) 722–733, <https://doi.org/10.1016/j.actamat.2018.12.013>.
- [12] L.C. Liu, H.R. Gong, Hydrogen solubility and diffusivity at  $\Sigma 3$  grain boundary of PdCu, RSC Adv. 11 (2021) 13644–13652, <https://doi.org/10.1039/DORA10133H>.
- [13] D.D. Stefano, M. Mrovec, C. Elsässer, First-principles investigation of hydrogen trapping and diffusion at grain boundaries in nickel, Acta Mater. 980 (2015) 306–312, <https://doi.org/10.1016/j.actamat.2015.07.031>.
- [14] V.P. Ramunni, M.I. Pascuet, N. Castin, A.M.F. Rivas, The influence of grain size on the hydrogen diffusion in bcc Fe, Comput. Mater. Sci. 188 (2021), 110146, <https://doi.org/10.1016/j.commatsci.2020.110146>.
- [15] A. Oudriss, J. Creus, J. Bouhattate, C. Savall, B. Peraudeau, X. Feaugas, The diffusion and trapping of hydrogen along the grain boundaries in polycrystalline nickel, Scr. Mater. 66 (2012) 37–40, <https://doi.org/10.1016/j.scriptamat.2011.09.036>.
- [16] A.M. Brass, A. Chanfreau, Accelerated diffusion of hydrogen along grain boundaries in nickel, Acta Mater. 44 (1996) 3823–3831, [https://doi.org/10.1016/1359-6454\(95\)00446-7](https://doi.org/10.1016/1359-6454(95)00446-7).
- [17] B. Ladna, H.K. Birnbaum, SIMS study of hydrogen at the surface and grain boundaries of nickel bicrystals, Acta Metall. 35 (1987) 2537–2542, [https://doi.org/10.1016/0001-6160\(87\)90150-7](https://doi.org/10.1016/0001-6160(87)90150-7).
- [18] T. Tsuru, R.M. Latanision, Grain boundary transport of hydrogen in nickel, Scr. Mater. 16 (1982) 575–578, [https://doi.org/10.1016/0036-9748\(82\)90273-3](https://doi.org/10.1016/0036-9748(82)90273-3).
- [19] M. Koyama, A. Bashir, M. Rohwerder, S.V. Merzlikin, E. Akiyama, K. Tsuzaki, D. Raabe, Spatially and kinetically resolved mapping of hydrogen in a twinning-induced plasticity steel by use of scanning kelvin probe force Microscopy, J. Electrochem. Soc. 162 (2015) 162, <https://doi.org/10.1149/2.0131512jes>, C638–C647.
- [20] A. Nazarov, F. Vucko, D. Thierry, Scanning kelvin probe for detection of the hydrogen induced by atmospheric corrosion of ultra-high strength steel,

- Electrochim. Acta 216 (2016) 130–139, <https://doi.org/10.1016/j.electacta.2016.08.122>.
- [21] R.F. Schaller, J.R. Scully, Measurement of effective hydrogen diffusivity using the scanning kelvin probe, Electrochim. Commun. 40 (2014) 42–44, <https://doi.org/10.1016/j.elecom.2013.12.025a>.
- [22] K. Ichitani, S. Kuramoto, M. Kanno, Quantitative evaluation of detection efficiency of the hydrogen microprint technique applied to steel, Corros. Sci. 45 (2003) 1227–1241, [https://doi.org/10.1016/S0010-938X\(02\)00218-4](https://doi.org/10.1016/S0010-938X(02)00218-4).
- [23] Z. Tarzimoghadam, M. Rohwerder, S.V. Merzlikin, A. Bashir, L. Yedra, S. Eswara, D. Ponge, D. Raabe, Multi-scale and spatially resolved hydrogen mapping in a Ni-Nb model alloy reveals the role of the  $\delta$  phase in hydrogen embrittlement of alloy 718, Acta Mater. 109 (2016) 69–81, <https://doi.org/10.1016/j.actamat.2016.02.053>.
- [24] M. Koyama, D. Yamasaki, T. Nagashima, C.C. Tasan, K. Tsuzaki, In situ observations of silver-decoration evolution under hydrogen permeation: effects of grain boundary misorientation on hydrogen flux in pure iron, Scr. Mater. 129 (2017) 48–51, <https://doi.org/10.1016/j.scriptamat.2016.10.027>.
- [25] H. Kakinuma, S. Ajito, T. Hojo, M. Koyama, E. Akiyama, Real-time visualization of hydrogen distribution in metals using polyaniline: an ultrasensitive hydrogenochromic sensor, Adv. Mater. Interf. 9 (2022) 2101984, <https://doi.org/10.1002/admi.202101984>.
- [26] H.-C. Lee, Color Imaging Science, Cambridge University Press, Cambridge, UK, 2005.
- [27] X. Zhou, N. Mousseau, J. Song, Is hydrogen diffusion along grain boundaries fast or slow? Atomistic origin and mechanistic modeling, Phys. Rev. Lett. 122 (2019), 215501, <https://doi.org/10.1103/PhysRevLett.122.215501>.
- [28] P.R.M. Van Beers, V.G. Kouznetsova, M.G.D. Geers, M.A. Tschoop, D.L. McDowell, A multiscale model of grain boundary structure and energy: from atomistics to a continuum description, Acta Mater. 82 (2015) 513–529, <https://doi.org/10.1016/j.actamat.2014.08.045>.
- [29] R. Dingreville, S. Berbenni, On the interaction of solutes with grain boundaries, Acta Mater. 104 (2016) 237–249, <https://doi.org/10.1016/j.actamat.2015.11.017>.
- [30] M. Zamanzade, C. Müller, J.R. Velayarce, C. Motz, Susceptibility of different crystal orientations and grain boundaries of polycrystalline Ni to hydrogen blister formation, Int. J. Hydrog. Energy 44 (2019) 7706–7714, <https://doi.org/10.1016/j.ijhydene.2019.01.263>.